Soft Matter

Covalently integrated silica nanoparticles in poly(ethylene glycol)-based acrylate resins: thermomechanical, swelling, and morphological behavior

Journal:	*Soft Matter*
Manuscript ID	SM-ART-09-2021-001377.R1
Article Type:	Paper
Date Submitted by the Author:	17-Dec-2021
Complete List of Authors:	Hocken, Alexis; Arizona State University, Chemical Engineering Beyer, Frederick; Army Research Laboratory Aberdeen Proving Ground Lee, Jae Sang; Arizona State University, Chemical Engineering Grim, Bradley; Arizona State University, Chemical Engineering Mithaiwala, Husain; Arizona State University, Chemical Engineering Green, Matthew; Arizona State University, Chemical Engineering

Covalently integrated silica nanoparticles in poly(ethylene glycol)-based acrylate resins: thermomechanical, swelling, and morphological behavior

Alexis Hocken[1], Frederick L. Beyer[2], Jae Sang Lee[1], Bradley J. Grim[1], Husain Mithaiwala[1], and Matthew D. Green[1,*]

[1]Department of Chemical Engineering; School for Engineering of Matter, Transport and Energy, Arizona State University, Tempe, AZ 85287, USA
[2]U.S. DEVCOM Army Research Laboratory, Aberdeen Proving Ground, MD 21005, USA

Keywords: photocurable nanocomposites, silica nanoparticles, PEG composites, functionalized nanoparticles

Abstract

Nanocomposites integrate functional nanofillers into viscoelastic matrices for electronics, lightweight structural materials, and tissue engineering. Herein, the effect of methacrylate-functionalized (MA-SiO_2) and vinyl-functionalized (V-SiO_2) silica nanoparticles on the thermal, mechanical, physical, and morphological characteristics of poly(ethylene glycol) (PEG) nanocomposites was investigated. The gel fraction of V-SiO_2 composites decreases upon addition of 3.8 wt% but increases with further addition (>7.4 wt%) until it reaches a plateau at 10.7 wt%. The MA-SiO_2 induced no significant changes in gel fraction and both V-SiO_2 and MA-SiO_2 nanoparticles had a negligible impact on the nanocomposite glass transition temperature and water absorption. The Young's modulus and ultimate compressive stress increased with increasing nanoparticle concentration for both nanoparticles. Due to the higher crosslink density, MA-SiO_2 composites reached a maximum mechanical stress at a concentration of 7.4 wt%, while V-SiO_2 composites reached a maximum at a concentration of 10.7 wt%.

Scanning electron microscopy, transmission electron microscopy, and small-angle X-ray scattering revealed a bimodal size distribution for V-SiO_2 and a monomodal size distribution for MA-SiO_2. Although aggregates were observed for both nanoparticle surface treatments, V-SiO_2 dispersion was poor while MA-SiO_2 were generally well-dispersed. These findings lay the framework for silica nanofillers in PEG-based nanocomposites for advanced manufacturing applications.

Introduction

Polymers are broadly used for many practical materials, such as biomedical implants, semiconductors, consumer products, and more.[1–4] The polymer modulus often dictates the characteristics for a given application, and while polymers have a range of moduli, the incorporation of different heterogeneous additives (i.e., to form polymer composites) can reinforce the polymer matrix and additionally improve optical characteristics, mechanical strength, conductivity, etc., while maintaining their characteristic lightweight nature.[2,3,5–7] Polymer composites have significantly impacted modern technology due to their multifunctionality and tunability.[8–10] Additives exist in a wide range of sizes and functionalities to enhance and fine-tune certain properties (often, a particular additive will be used to impart a specific property).[11–15] For example, fiberglass can be integrated to enhance durability and structural integrity, while carbon nanotubes are used to improve electrical conductivity of materials.[9,16] Furthermore, TiO_2 nanoparticles can be added to refine optical quality.[17] A setback of nanoadditives is the control over dispersion as additives are prone to aggregation, thereby impacting the composite's material properties.[18,19] However, Kumar et al. stated that thermodynamic miscibility of the nanoparticles with polymers can be improved by using nanoparticle surface ligands that are chemically similar to the melt and polymer chains with lower molecular weights.[2,18] The challenges associated with obtaining sufficient nanoadditive dispersion leads to a sub-maximal functional benefit of the additive which is a significant trade-off.

Polymer networks can be formed using a variety of synthetic pathways; those formed via step growth polymerizations are the oldest and helped define many of the network formation theories.[20–22] Advances in polymer synthesis techniques have carried over to network synthesis,

with click chemistry, photochemistry, renewable polymers, and free radical chemistries being utilized.[20,21,23] To make these networks even more versatile and functional, nanoadditives can be incorporated to make nanocomposites.[24,25] As an example, Hata et al. demonstrated the benefit of adding silica nanoparticles to their step growth thiol-ene systems to improve holographic storage for media.[26] Free radical polymerization can also be used to form physical networks by the sequential addition of monomer building blocks to make block polymers; block polymers have distinct microdomains that can selectively solubilize nanoparticles with different surface functionalities.[27,28] Polymer nanocomposites can also be prepared by dispersing nanoparticles in a monomer or oligomer solution and then crosslinking the resin, often through the use of photoreaction or photopolymerizations.[29–31] Photocurable reaction schemes offer spatial control, which makes them attractive candidates to build hierarchically structured materials (e.g., metamaterials, composites, etc.) or 3D materials with custom and pre-programmed shapes (e.g., dental fillings, tissue implants, etc.).[29,32–35] Upon the addition of photoinitiators and exposure to light, the formation of stable, covalently bonded crosslinks occurs between monomers.[29,36,37]

Several studies have investigated the influence of silica nanoadditives on the composite properties for use in applications such as automobile tires, electrical products, and coatings.[38–43] Dizon et al. analyzed the thermomechanical properties of 3D-printed nanocomposites to be used as biomedical and microfluidic devices and discovered that increasing the loading of silica nanoparticles lead to higher stiffness.[32] Earlier work from our laboratory noted that nanocomposites containing unfunctionalized SiO_2 nanoparticles exhibited the behavior that the addition of particles caused the composite's Young's modulus and ultimate compressive stress to increase by 2x and 3x, respectively.[44] The high modulus SiO_2 nanoparticles stiffen the matrix around it by limiting mobility, which increases the modulus and contributes to a more robust

material. Others have noted that the increase in modulus is dictated by the interfacial area, where a higher additive surface area leads to a stiffer matrix.[45] Theoretically speaking, the modulus could increase infinitely with increasing loading of additives in a perfectly mixed system, however particle agglomeration and/or percolation leads to a trade-off wherein further nanoparticle additions degrade the mechanical properties of the composite.[46] These previous studies demonstrate the tunability of the thermal and mechanical properties of SiO_2-loaded composites. However, the percolation and agglomeration occurred at too low of a concentration, resulting in too modest of functional gains to be translated to any practical applications. To increase the range of properties that can be achieved, it would be beneficial to explore nanoscale additives with alternative surface functionalities that can be incorporated into the polymer matrix of the composite.

Functionalized nanoparticles offer a solution to limited gel fractions and particle agglomeration. For example, Schneider et al. used gold nanoparticles coated with polyelectrolytes that allowed them to tailor the ionic strength, polyelectrolyte contour length, and concentration of polyelectrolyte to limit particle aggregation and improve dispersion in ultrathin composite films.[47] Functionalized nanoparticles can participate in the cross-linking reaction (i.e., with a reactive functional group that complements the matrix chemistry) and compensate for losses in monomer crosslinks.[48] This strategy was utilized in a study conducted by Rossi et al. wherein functionalized polymeric nanoparticles were crosslinked within a polymer hydrogel to control the biodegradability of the material.[48] Silica-based nanocomposites fabricated with functional, or reactive, surface chemistries have also been studied extensively.[49–53] Wang et al. prepared double-network hydrogels wherein vinyl-coated silica nanoparticles were copolymerized with 2-acrylamido-2-methylpropanesulfonic acid and N,N'-

methylenebis(acrylamide) (MBAA) to make a first network followed by the addition of a second network comprised of acrylamide and MBAA.[54] Silica nanoparticle concentrations of only <4 wt% were studied, but the authors observed the formation of a hierarchical microstructure that resulted in resilient mechanical properties. In another study, Bauer et al. loaded up to 35 wt% of silica nanoparticles bearing different trialkoxysilane functional groups and noted that the vinyl and methacrylate reactive groups markedly improved the surface abrasion resistance.[55] The functional surface groups can improve mechanical integrity as above, but also have the potential to improve nanoparticle dispersion in the composite when mixed with chemically similar monomers. In summarizing this work, we observed a couple of gaps in the literature. The nanocomposite morphology (i.e., nanoparticle dispersion) across the broad range of nanoparticle concentrations and the connection between the reactive functional group chemistry and the bulk thermomechanical properties were not studied.

In this study, SiO_2 nanoparticles containing vinyl- and methacrylate-functional groups (V-SiO_2 and MA-SiO_2, respectively) were used as nanofillers in a polymeric composite (**Figure 1**). SiO_2 nanoparticles are commonly used in nanocomposites due to their low cost, tunable surface chemistry, and other interesting properties including high mechanical strength and thermal and chemical stability.[56] These nanoparticles were loaded into in a model photocurable polymer nanocomposite system composed of a poly(ethylene glycol) diacrylate matrix. The V-SiO_2 and MA-SiO_2 nanoparticles were loaded at five different weight fractions (0, 3.8, 7.4, 10.7, and 13.8 wt%) to study the impact they have on the gel fraction, glass transition temperature (T_g), and the static and dynamic strain rate mechanical properties. Additionally, the water uptake, surface and cross-section morphology, and thermal stability were determined. Small-angle X-ray scattering (SAXS) experiments, conducted to determine the nanoparticle size and size

distribution, corroborated findings from electron microscopy experiments. Static strain rate compression testing was used to characterize the Young's modulus, the ultimate compressive stress, and the ultimate compressive strain at break. This research probes the potential of utilizing functionalized SiO_2 nanoparticles to build a database of properties and characteristics that allow for pinpoint, desired qualities in a material amenable to additive and advanced manufacturing techniques.

Figure 1. Schematic showing a) unfunctionalized and inert SiO_2 nanoparticles, b) methacrylate-functionalized nanoparticles (MA-SiO_2), and c) vinyl-functionalized nanoparticles (V-SiO_2). V-SiO_2 nanoparticles are functionalized with vinyl and alkyl groups where "n" is unknown. The vinyl concentration is also unknown.

Experimental

Materials

The poly(ethylene glycol) diacrylate (PEGDA, M_n = 575 g/mol, purity of ≥99.68%) and 2-dimethoxy-2-phenylacetophenone (DMPA) were purchased from Sigma-Aldrich and used without further purification. The methacrylate-functionalized (MA-SiO_2) and vinyl-functionalized (V-SiO_2) silicon dioxide nanoparticles (100 nm in diameter) were purchased from NanoCym and used as received. Although, later analysis revealed that the particle size

distribution was not monomodal. Tetrahydrofuran (THF) was purchased from Fisher Chemical and purified using an MBraun solvent purification system.

Composite Fabrication

The process to prepare silica-loaded nanocomposites was adapted from our previous protocols.[44] Composite samples were made by loading MA-SiO_2 into PEGDA. To reduce MA-SiO_2 aggregation, the nanoparticles were first dispersed in THF (0, 0.04, 0.08, 0.12, or 0.16 g of SiO_2 was added to 3 mL THF) and sonicated for 40 min. Separately, DMPA was mixed with the PEGDA at a ratio of 0.0035:1 w/w (DMPA:PEGDA) based on a previous optimization study.[44] The THF solution was then pipetted into 1.0 g of the DMPA/PEGDA mixture and stirred at 23 °C for 45 min. Next, the THF was evaporated at 23 °C and the solution was transferred into a silicone mold and cured under a MelodySusie UV Gel Nail Polish Dryer UV light (Model DR-301C, wavelength (λ) of ~365 nm) for 3 min. The weight fraction of functionalized nanoparticles in a given composite includes the weight of the silica and the functional ligands. A sample calculation for the 3.8 wt% MA-SiO2 samples are shown in Equation 1:

$$W\ (\%) = \frac{0.04\ g\ MA-SiO_2}{0.04\ g\ MA-SiO_2 + 1.0\ g\ DMPA/PEGDA\ mix} \times 100 = 3.8\ wt\%\ MA-SiO_2$$

The same process was used to fabricate composites containing V-SiO_2 nanoparticles.

Determination of Sol−Gel Fractions

Soxhlet extraction was used to determine gel fractions. A pre-weighed sample was placed in the apparatus and >12 complete solvent wash cycles were completed. THF was used as the solvent to dissolve any remaining soluble fraction. The sample was then weighed again after drying under vacuum overnight at 25 °C to determine the final mass (W_f), which was compared

to the initial mass (W_i). Three replicates were performed for each sample type. The gel fraction (C) was calculated according to Equation 2:

$$C\ (\%) = \frac{W_f}{W_i} \times 100 \quad (1)$$

Water Uptake Experiments

In a standard process, the sample was oven-dried at 100 °C and atmospheric pressure for 14 h to ensure all water that was absorbed from atmospheric moisture was removed. Water uptake was performed for >3 hours based on previously developed protocol.[44] An experiment to confirm the water uptake equilibrium time was conducted (See **Figure S1**). The samples were weighed and immersed in deionized water for at least 3 h to reach the absorption equilibrium. The sample was removed from the water and blotted with a cloth to remove excess water on the surface. This sample's wet mass (W_s) was recorded and compared to its initial dry mass (W_d). The percentage (by weight) of water taken up by the network (S) was calculated using Equation 3:

$$S\ (\%) = \frac{W_s - W_d}{W_d} \times 100 \quad (2)$$

Thermal stability tests

Thermogravimetric analysis (TGA) was performed using a TA Instruments TGA5500. Samples (~5 mg each) were heated at a rate of 10 °C/min from 23-600 °C under nitrogen.

Scanning Electron Microscopy

The composite surface and cross-sectional morphology was characterized using a FEI Nova 200 NanoLab field emission scanning electron microscopy (SEM) system. The accelerating voltage was set to 10 kV with a probe current of 0.54 – 2.1 nA using the Everhart Thornley detector (ETD) at a working distance (WD) of 5.0 mm. Composite samples were

freeze-fractured using liquid nitrogen for surface and cross-sectional imaging. All samples were imaged using a consistent sample thickness of ~4 mm.

Atomic Force Microscopy

Atomic force microscopy (AFM) was performed using a Bruker MultiMode 8. AFM was equipped with microcantilever tip (NCHV-A) for tapping mode at room temperature.

Transmission Electron Microscopy

Transmission electron microscopy (TEM) of the silica nanoparticles was performed using a Phillips CM200-FEG that was operated at 200 keV in bright-field mode. Micrographs were collected using an ORIUS CCD Model 831.P2020 camera (Gatan, Inc.). Samples of SiO_2 nanoparticles were prepared by drop casting nanoparticle dispersions in either methanol or THF onto carbon-coated TEM grids. The nanoparticle dispersions were made by hand mixing SiO_2 powder in the desired solvent, then dispensed using a micropipette. TEM on the nanocomposite samples was performed on a JEM-2100F TEM (JEOL USA, Inc.) operated at 200 kV accelerating voltage. Bright field images were captured using an ORIUS SC1000 CCD camera (Gatan, Inc.) on 200 nm thick, 100-200 μm wide sections microtomed at -40 °C using a Leica UC7 cryo-ultramicrotome.

Small-Angle X-ray Scattering

SAXS data were collected on the combined ultra-small-angle X-ray scattering (USAXS), SAXS, and wide-angle X-ray scattering (WAXS) instrument at the Advanced Photon Source (APS) of the Argonne National Laboratory (Lemont, Illinois, USA). The instrument has been described in detail elsewhere, and was used in the standard instrumental configuration.[57] The incident photon energy was 21 keV, giving a wavelength (λ) of 0.5904 Å. Raw data were corrected for instrument background, sample transmission, and detector solid angle, and scaled

to absolute intensity. The combined data span an angular range of q = 0.000114 Å^{-1} to 1.723 Å^{-1}, where q is the magnitude of the scattering vector, defined as ($4\pi \cdot \sin(\theta)/\lambda$), where 2θ is the scattering angle. All data corrections, manipulation, and analysis were performed using Igor Pro v7 (Wavemetrics, Inc.) and procedures developed at the Argonne National Laboratory and the National Institute for Standards and Technology for this purpose.[58–60]

Thermal and Mechanical Analysis

The glass-transition temperature (T_g) was characterized using differential scanning calorimetry (DSC, Q2000, TA Instruments). Samples of 4−6 mg were sealed into aluminum sample pans. The samples were subjected to a heat−cool−heat process from −90 °C to 200 °C with heating rates of 5 °C/min and a cooling rate of 10 °C/min. The midpoint T_g was determined using the T_g function built into TA Instruments' TRIOS 5.1.1 software. An Instron E3000 was used to perform compression testing of the nanocomposites. A fresh, dry sample was used for each test. The samples were cut into rectangles and then compressed at a strain rate of 0.1500 mm/min at 23 °C until the sample integrity was compromised. Dynamic mechanical analysis (DMA) was performed to characterize the viscoelastic behavior of the material with a Discovery HR-2 hybrid rheometer (TA Instrument) in tension mode at from -80 °C to 120 °C with heating rates of 3 °C/min and a frequency of 1 Hz.

Results and Discussion

Synthesis and Characterization

Photocurable acrylates have been used in dentistry and other applications because of the fast-curing kinetics, favorable viscoelastic properties, and the ability to tune color. **Scheme 1a** shows the reaction pathway to cure an oligomeric diacrylate (PEGDA) using a photoinitiator. The addition of functionalized nanoparticles introduces a new type of interaction in the matrix that

allows for covalent bonds to form between the surface groups on a nanoparticle and a PEGDA monomer. This synthetic route, for both MA-SiO_2 and V-SiO_2 nanoparticles, is illustrated in **Scheme 1b** and **Scheme 1c**, respectively. The manufacturer reported the nanoparticle diameter as 100 nm for all surface chemistry. The insertion of functionalized groups on the nanoparticle surface enables material characteristics that can more precisely alter the molecular weight between crosslinks as well as maintain a high gel fraction because the fillers now participate in the crosslinking rather than inhibit it.

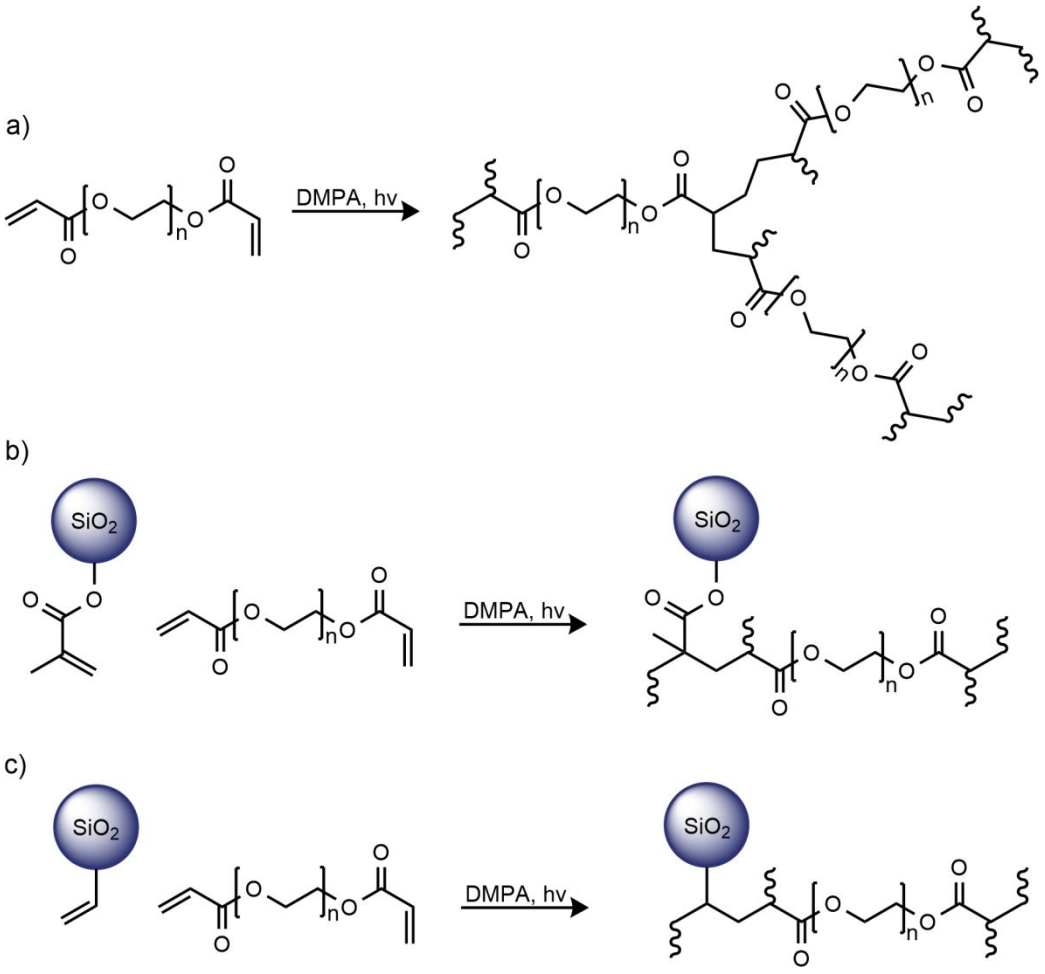

Scheme 1. Cross-Linking Reaction by DMPA under UV Light of a) PEGDA, b) PEGDA with MA-SiO_2 and c) PEGDA with V-SiO_2.

V-SiO_2 and MA-SiO_2 nanoparticles were added at various weight fractions and the PEGDA oligomers were cured. The gel fractions of the nanocomposites were measured at each nanoparticle concentration. As discussed in our previous study, the unfunctionalized SiO_2 nanoparticles cause a decrease in the gel fraction with the addition of 3.8, 7.4, and 10.7 wt%.[44] However, further addition of nanoparticles to achieve 13.8 wt% resulted in no statistically significant changes.[44] Unlike the unfunctionalized SiO_2 nanoparticles, the increasing weight fractions of V-SiO_2 and MA-SiO_2 do not cause a decrease in gel fraction. **Figure 2** demonstrates that the gel fraction for MA-SiO_2 stays constant with an increase in nanoparticle loading (at ~97%) and the differences between gel fraction at the varying MA-SiO_2 loadings are not statistically significant with a p-value >0.05. This suggests that the MA-SiO_2 nanoparticles do not hinder the crosslinking reaction as the loading is increased, supporting the idea that the MA-SiO_2 particles participate in the polymerization. While the PEGDA content is diluted in the composite due to the addition of nanoparticles, the gel fraction does not change significantly. This means that the particle-monomer crosslinks are compensating for the loss in monomer-monomer crosslinks. The trend for the V-SiO_2 composite series was slightly different. The addition of 3.8 wt% V-SiO_2 causes an initial decrease in gel fraction to ~95%. This reduction in gel fraction suggests that V-SiO_2 initially inhibits cross-linking by potentially scavenging radicals and/or limiting monomer diffusion. We hypothesize that the addition of nanoparticles inhibits light penetration to the entire composite resin and produces isolated or localized networks, which results in a lower gel fraction at the lowest nanoparticle loading.[61,62] Further increases in V-SiO_2 nanoparticles (e.g., 7.4 and 10.7 wt% of V-SiO_2) cause an increase in the gel fraction, suggesting that the functional end groups contribute to the polymerization at the higher loadings more than they inhibit it. In other words, since there is a higher reactive group

concentration at higher loadings (i.e., methacrylate and/or vinyl groups), the hampered crosslinking seen at low loadings was overcome. Once the weight fraction of V-SiO_2 exceeds 10.7 wt%, no statistically significant change in gel fraction is observed with a p-value >0.05.

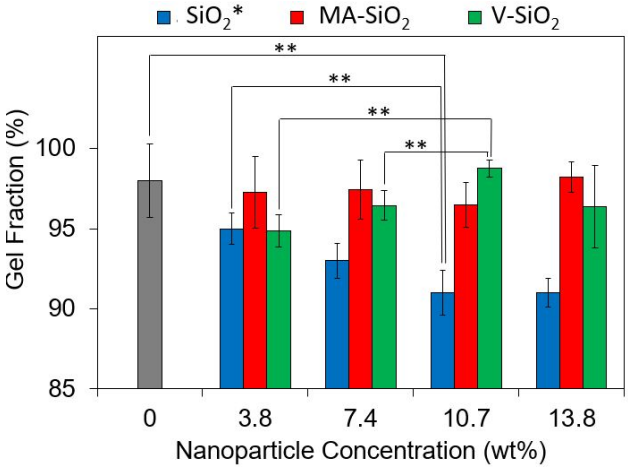

Figure 2. Gel fraction of PEGDA networks with varying MA-SiO_2 and V-SiO_2 weight fractions in comparison to unfunctionalized[44] SiO_2. Error bars represent the mean of 3 replicates ± one standard deviation. Statistically significant changes are denoted by **.

Thermal analysis using TGA was performed to determine the thermal stability and quantitatively measure the nanoparticle loading in the nanocomposites (**Figure 3**). A single decomposition step was revealed at ~360 °C for both the V-SiO_2 and MA-SiO_2 loaded nanocomposites. For V-SiO_2 loaded composites, sharp weight losses of 90.1, 86.9, 85.5, and 84.5 wt% were observed as the loading of nanoparticles increased from 3.8 to 13.8 wt%. For the MA-SiO_2 loaded composites, sharp weight losses of 90.1, 87.7, 84.7, and 83.5 wt% occurred as the loading of particles increased from 3.8 to 13.8 wt%. The sharp decomposition step is attributed to the degradation of PEG polymer matrix. The nanoparticles concentrations were calculated for each sample series accounting for the char weight of the PEGDA matrix. It was estimated that the MA-SiO_2 nanocomposite series had weight percentages of 3.8, 6.1, 9.0, and 11.5 wt% for the 3.8, 7.4, 10.7, and 13.8 wt% samples, respectively. The weight percentages were 3.2, 5.8, 8.1, and 8.2 wt% for the 3.8, 7.4, 10.7, and 13.8 wt% V-SiO_2-loaded nanocomposite samples,

respectively. These TGA data confirm the increasing trend in nanoparticle loading across each nanocomposite series. However, it is noted that the 10.7 and 13.8 wt% V-SiO_2 nanocomposite samples have nearly identical degradation curves, resulting in similar calculated weight fractions of 8.1 and 8.2 wt%. We posit that this is due to the composite reaching its solubility limit causing the nanocomposite to exceed the threshold in which it can support nanoparticles. This phenomenon is corroborated in TEM data to follow.

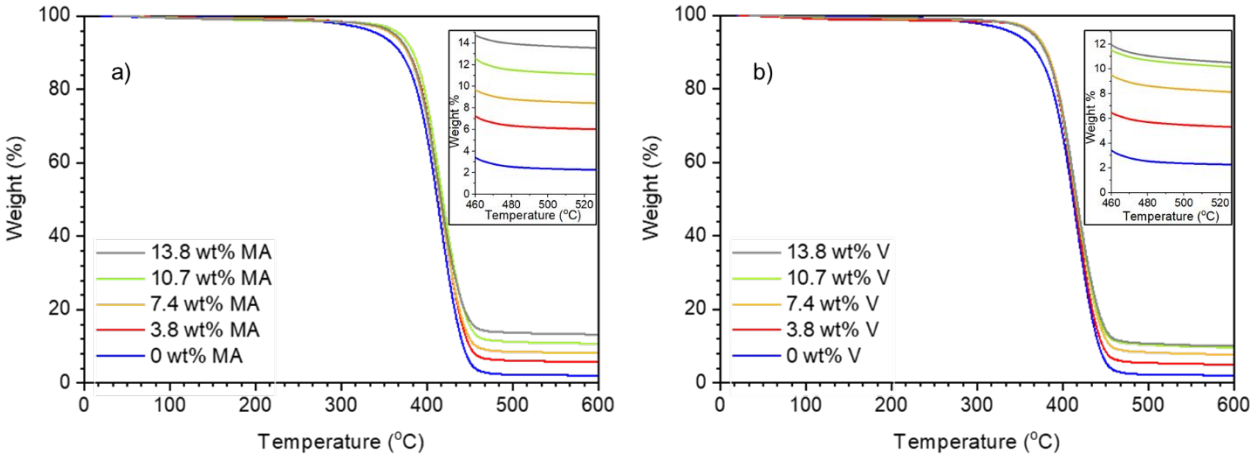

Figure 3. TGA thermograms showing weight loss from thermal decomposition of the a) MA-SiO_2 loaded and b) V-SiO_2 loaded PEGDA nanocomposites.

Composite Morphology

The cross-section morphologies of both MA-SiO_2 and V-SiO_2 nanocomposites (**Figure 4**) were examined using SEM. In general, the MA-SiO_2 nanocomposites exhibited good nanoparticle dispersion at all concentrations. Qualitatively, the concentration of dispersed MA-SiO_2 nanoparticles increased as the weight fraction increased. Aggregates 1-3 μm in diameter were observed at all concentrations, with a slight increase in the number of aggregates observed with increasing NP content. The V-SiO_2 nanocomposites were observed to contain large aggregates many microns in size at all NP concentrations, beginning with the initial introduction of 3.8 wt% nanoparticles. With further addition (>3.8 wt%) more aggregation and larger

aggregates were observed. It was noted that the V-SiO_2 composites have fewer dispersed nanoparticles. The micrographs highlight the non-porous nature of the nanocomposites, indicating that residual solvent from the preparation process was not present. Images of the surfaces of all the composites (see examples in **Figure S2**) revealed a surface layer of nanoparticles, suggesting incomplete dispersion at all concentration levels.

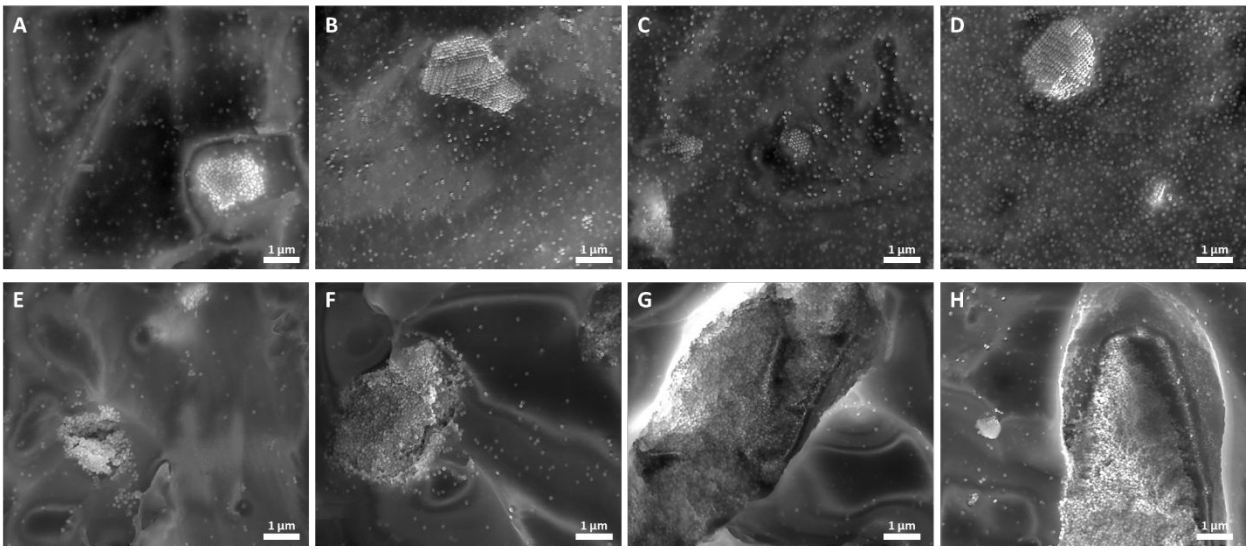

Figure 4. Cross-sectional SEM images of the series of composites with A) 3.8 wt%, B) 7.4 wt%, C) 10.7 wt%, and D) 13.8 wt% MA-SiO_2 as well as E) 3.8 wt%, F) 7.4 wt%, G) 10.7 wt%, and H) 13.8 wt% V-SiO_2.

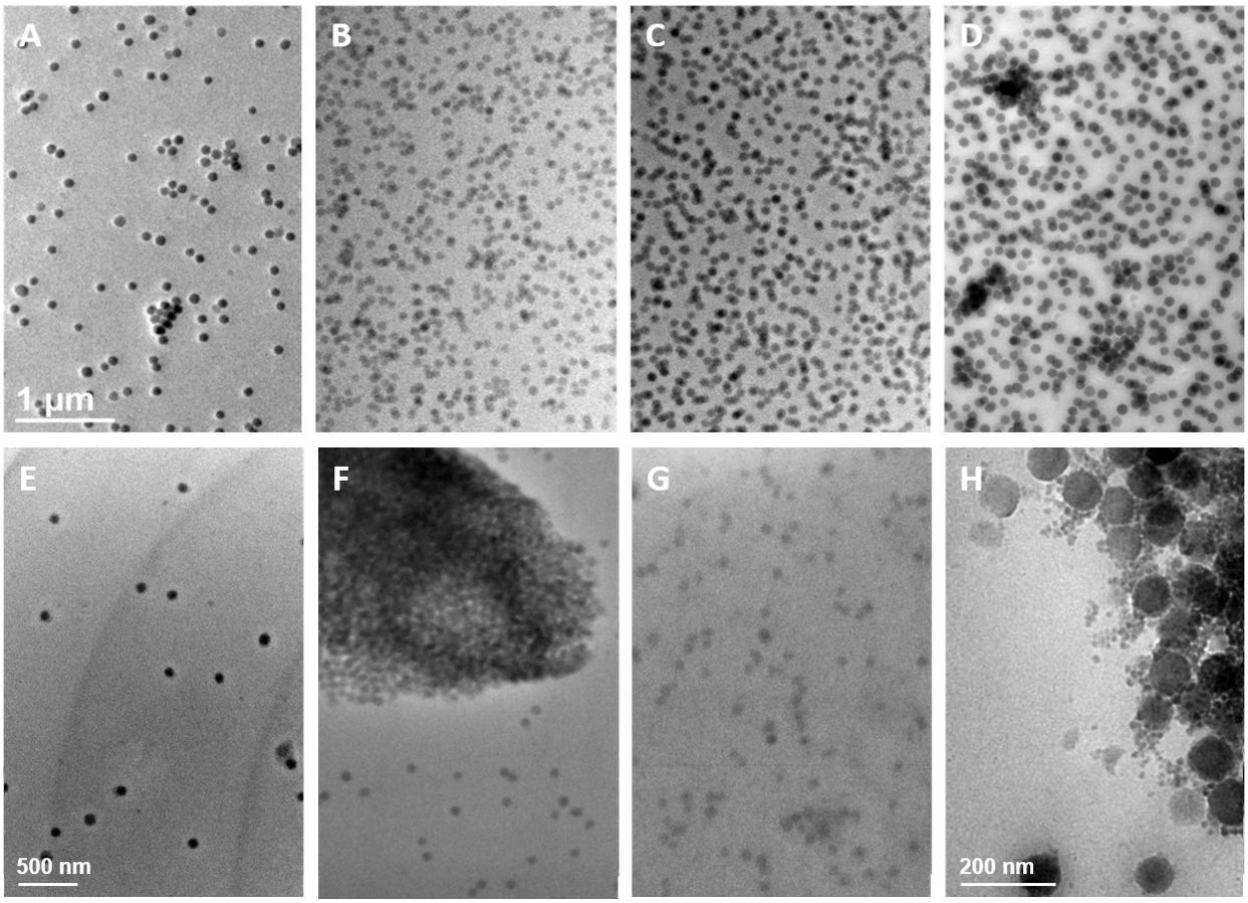

Figure 5. TEM micrographs of the composites having A) 3.8 wt%, B) 7.4 wt%, C) 10.7 wt%, and D) 13.8 wt% MA-SiO_2 as well as E) 3.8 wt%, F) 7.4 wt%, G) 10.7 wt%, and H) 13.8 wt% V-SiO_2. Images B, C, and D have been scaled to match the magnification of image A. Images F and G have been scaled to match the magnification of image E. Image H is enlarged to illustrate the bimodal size distribution of nanoparticles in the V-SiO_2 samples.

Figure 5 shows representative TEM micrographs for all eight composite compositions. Micrographs from the MA-SiO_2 composites are shown in images A-D, while those from the V-SiO_2 composites are shown in images E-H. Nanoparticle content increases moving from left to right in the figure, as loading increases from 3.8 wt% to 13.8 wt%. The TEM data show that, in general, the MA-SiO_2 nanoparticles are dispersed very well throughout the composition range, although small aggregates were observed in all four samples. The MA-SiO_2 nanoparticles appear to be roughly 100 nm in diameter. In contrast, the TEM data showed that the V-SiO_2

composites all contained very large aggregates, such as the one shown in **Figure 5F**. These aggregates were often many microns in size. Although the overall content of SiO_2 nanoparticles increased with loading up to a concentration of 10.7 wt% V-SiO_2 (as noted in the TGA data), the loading observed outside of the aggregates was significantly lower than that observed for the samples containing methacrylate-functionalized nanoparticles, consistent with the formation of the large aggregates. The TEM data also corroborate the solubility limit that was projected in the TGA results as severe aggregation was observed in the 13.8 wt% V-SiO_2 sample. To illustrate nanoparticle size, **Figure 5H** is presented at a higher magnification and shows not only large V-SiO_2 particles approximately 90 nm in diameter, but also numerous small nanoparticles roughly 15 nm in diameter. This suggests the vinyl-functionalized nanoparticles have a bimodal size distribution.

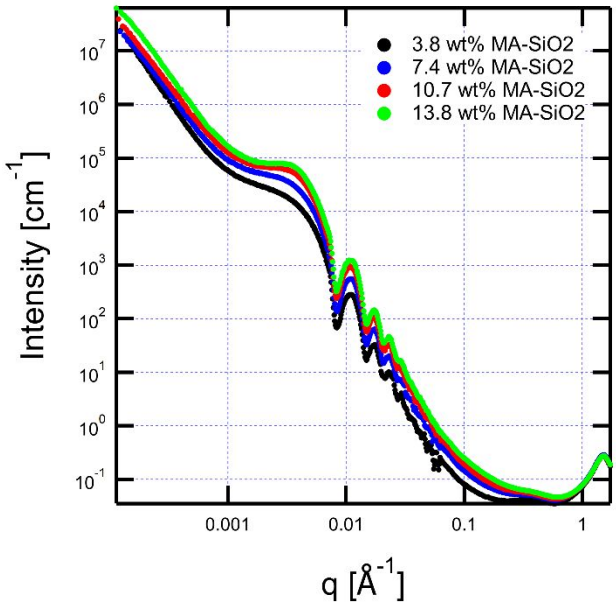

Figure 6. SAXS data for the MA-SiO_2 nanocomposites with varying concentrations of MA-SiO_2.

Figure 6 shows the SAXS collected for the four samples containing the MA-SiO_2 nanoparticles, with several distinct features visible. First, at the very lowest angles power law

scattering is observed with intensity scaling roughly as q^{-3}, indicating the presence of very large features in the sample with relatively rough edges.[63,64] This is consistent with the presence of micron-sized aggregates such as those observed in the SEM data (**Figure 4**). Atomic force micrographs (see **Figure S8**) show large aggregates with surface roughness on the order of 100 nm that would produce Porod Law scattering where intensity scales as q^{-3}.[65] Beginning at $q \approx 0.001$ Å^{-1} and extending up to $q \approx 0.1$ Å^{-1}, the data show form factor scattering comprising a large primary feature, commonly called the Guinier "knee,"[66] and a series of well-defined peaks decreasing in intensity with increasing q. This scattering is analyzed below. Finally, at higher angles, a weak polymerization peak was observed at $q \approx 0.4$ Å^{-1} and the amorphous halo is clearly visible at $q \approx 1.5$ Å^{-1}.[63] The overall scattering intensity is observed to increase with increasing SiO_2 nanoparticle content, as expected.

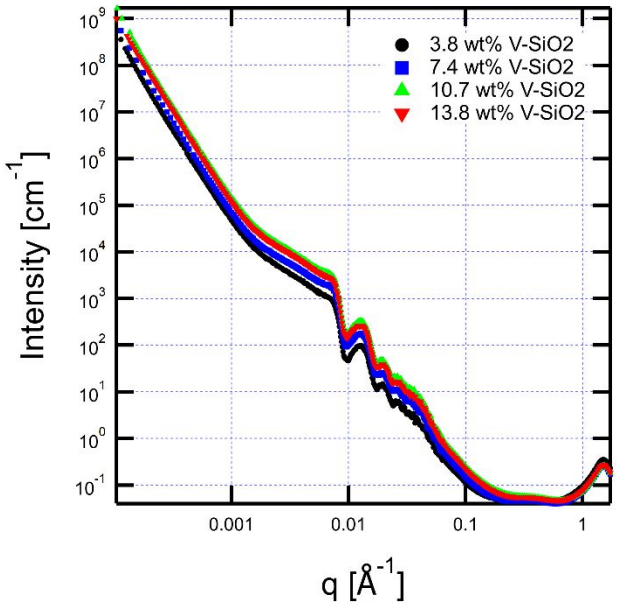

Figure 7. SAXS data for nanocomposites containing varying concentrations of V-SiO_2.

Figure 7 shows the SAXS data collected for the V-SiO_2 composites containing increasing loadings of V-SiO_2 nanoparticles. Notable differences to the data in **Figure 6** can be

observed. First, the lowest q data show a power law dependence of q^{-4}, rather than the q^{-3} dependence observed for the methacrylate-functionalized samples, indicating the presence of large features with smooth surfaces. This change is consistent with the observation of aggregates comprising a bimodal distribution of nanoparticles such as shown in **Figure 5H**, with the smaller NPs filling the gaps between larger particles to create a relatively smooth particle surface (see also AFM images in **Figure S8**) . Second, the first part of the form factor scattering observed between $q \approx 0.002$ Å^{-1} and 0.03 Å^{-1} appears to decrease linearly into a sharp drop in intensity around $q \approx 0.008$ Å^{-1}, rather than the plateau and then smooth drop seen in **Figure 6**. This drop is followed again by several peaks, but then a second Guinier knee feature is observed around $q \approx 0.05$ Å^{-1}. This feature is followed then by the same combination of the weak polymerization peak and amorphous halo seen for the MA-SiO_2 composites, originating from intermolecular and intramolecular scattering from the PEG matrix.[63]

The SAXS data were analyzed starting with the understanding that an amorphous polymer had been modified with a particulate material with particle sizes around 100 nm. The analysis of nanocomposites of this type is well established, and SAXS is a primary tool for characterization of these materials because it provides information on both the additive and the dispersion of the additive in the bulk.[67–69] Scattering from disordered two-phase materials is the combination of form factor scattering, $P(q)$, which is a function of the shape of the particles, and structure factor scattering, $S(q)$, which is due to interparticle interference, as described in Equation 3, where N is the number of scattering objects or domains.

$$I(q) = NP(q)S(q) = NB^2(q) \quad (3)$$

In the case of dilute scattering domains, the structure factor becomes 1. Furthermore, $P(q)$ is the square of the scattering amplitude, $B(q)$, which is the Fourier transform of the scattering length

density, ρ, throughout the particle, as given in Equation 4. Here r is the correlation length in real space and ρ_0 is the mean scattering length density throughout the sample.[70]

$$B(q) = 4\pi\int_0^\infty [\rho(r) - \rho_0]\frac{\sin qr}{qr} r^2 dr \quad (4)$$

As the concentration of particles or domains increases, interparticle scattering begins to affect the measured scattering. The effects of these interactions on the measured intensity can be modeled using the Percus-Yevick hard sphere structure factor.[71]

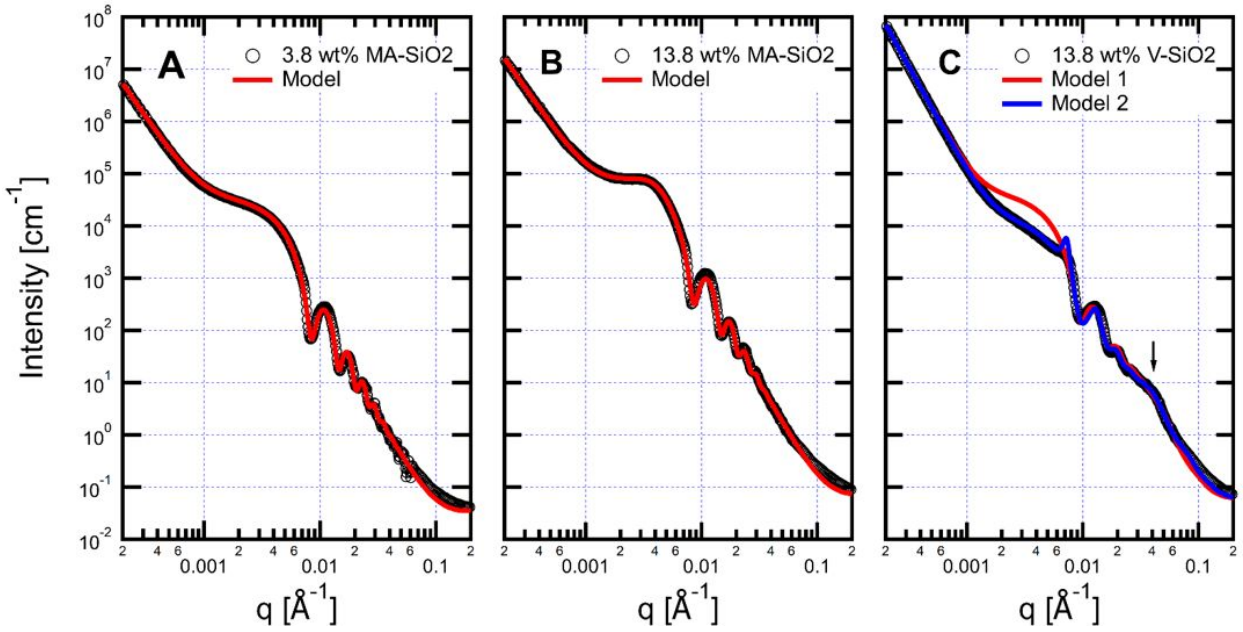

Figure 8. SAXS data for nanocomposites containing A) 3.8 wt% methacrylate-functionalized SiO_2, B) 13.8 wt% methacrylate-functionalized SiO_2, and C) 13.8 wt% vinyl-functionalized SiO_2. The results of model fitting to the data are shown in red and blue.

Figure 8 shows the results of least squares fitting of form factor scattering for the samples containing 3.8 wt% MA-SiO_2, 13.8 wt% MA-SiO_2, and 13.8 wt% V-SiO_2. For all modeling, a power law was used for the low-q data, and two peaks were used to account for the polymer scattering at high q (not shown). The middle region of the SAXS data was fit with combinations of form factor scattering from spherical particles and the Percus-Yevick hard

sphere structure factor. For the data from the 3.8 wt% MA-SiO_2 sample (**Figure 8A**) and the 13.8 wt% MA-SiO_2 sample (**Figure 8B**), the model scattering includes form factor scattering for a sphere 104 nm in diameter with a standard deviation of 5.9 nm. For the 3.8 wt% MA-SiO_2 loading, no evidence of interparticle scattering is seen, and the data are fit well using the form factor only. As the loading of silica nanoparticles increases, the shape of the Guinier knee between $q \approx 0.001$ $Å^{-1}$ and 0.01 $Å^{-1}$, gradually changes due to increased interparticle scattering, as can be seen in **Figure 8B** and in **Figure 6**. This change is captured well by the addition of the hard sphere structure factor.

Figure 8C shows the scattering and model fit for the nanocomposite containing 13.8 wt% V-SiO_2. As was noted in the TEM data (**Figure 6**), not only did the samples containing this nanoparticle show large scale aggregates, but they also showed the presence of smaller particles approximately 15 nm in diameter. The model fits to the SAXS data reported in **Figure 7** bear out these two observations. First, the power law behavior at the lowest angles shows a power law dependence of q^{-4}, indicative of a well-defined matrix-particle interface. Such an interface could be formed in aggregates of large and small particles, where the small particles fill voids between large particles. AFM data collected on a large aggregate in V-SiO_2 composite (see **Figure S8**) shows this kind of surface. Second, fitting the general shape of the form factor scattering in the Guinier region is not possible with only form factor scattering from large nanoparticles. The model fit shown in red in **Figure 8C** combines form factors for both large nanoparticles (93 nm diameter, 8.1 nm standard deviation) and small nanoparticles (12 nm diameter, 2.6 nm standard deviation). This model successfully captures the form factor fringes for the large size distribution, and the Guinier knee present at $q \approx 0.04$ $Å^{-1}$ (black arrow), but not the scattering observed in the Guinier region of the large nanoparticles. An improved fit (blue

trace in **Figure 8C**) to the unusual scattering in the Guinier region of the large nanoparticles was obtained by adding scattering from a third population of nanoparticles, having the same size distribution as the large nanoparticles (93 nm diameter) but including structure factor scattering. This improves the fit in the Guinier region with the exception of a sharp correlation peak at $q \approx 0.007$ Å^{-1}. Although this fit is imperfect, it suggests that the observed scattering is a complex combination of scattering from not only the two different nanoparticle sizes and distributions, but also interparticle scattering and scattering from the aggregates. A table of the fitting parameters for all samples is included in the SI.

Thermal and Mechanical Analysis of the Composites

Water uptake experiments were conducted to probe the composite hydrophilicity and swelling behavior as a function of nanoparticle concentration. Given hydrophobicity of silica, there was a concern that this hydrophobic property might translate over to the composite as a whole. The results depicted in **Figure 9** demonstrate that the hydrophilic nature of the composite is not dependent on the loading of nanoparticles for both Ma-SiO_2 and V-SiO_2. The water uptake percentage does not significantly change as the loading of nanoparticles increases. Similarly, these data suggest that the swelling behavior of the network does not vary significantly with nanoparticle concentration. This suggests that the hydrophobic nature of silica does not considerably impact the water uptake capabilities of PEGDA.

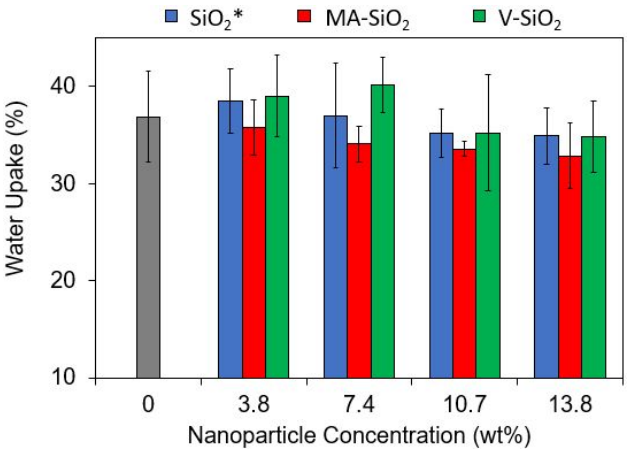

Figure 9. Water uptake measured gravimetrically at various nanoparticle weight percentages of SiO_2,[44] MA-SiO_2, and V-SiO_2. Error bars indicate the mean ± one standard deviation.

The glass transition temperature (T_g) was analyzed for each composite to elucidate the effects of the nanoparticle concentration on the composite thermal properties. For both series of nanocomposites, the loading of nanoparticles did not induce a statistically significant change in T_g (**Figure 10**). The composites containing MA-SiO_2 consistently display a higher T_g than the PEGDA network without any added nanoparticle. The initial addition of MA-SiO_2 particles causes a ~2 °C increase in T_g. From there, the T_g does not fluctuate more than 1 °C overall with further addition of MA-SiO_2 particles. For V-SiO_2 nanoparticles, the T_g decreases by ~1 °C with the initial incorporation of 3.8 wt% nanoparticles. With the addition of ≥7.4 wt% nanoparticles, the T_g steadily increases to -20.8 °C. These data corroborate the gel fraction data, wherein the initial addition of V-SiO_2 nanoparticles decreased gel fraction while further additions ≥7.4 wt% increased the gel fraction.

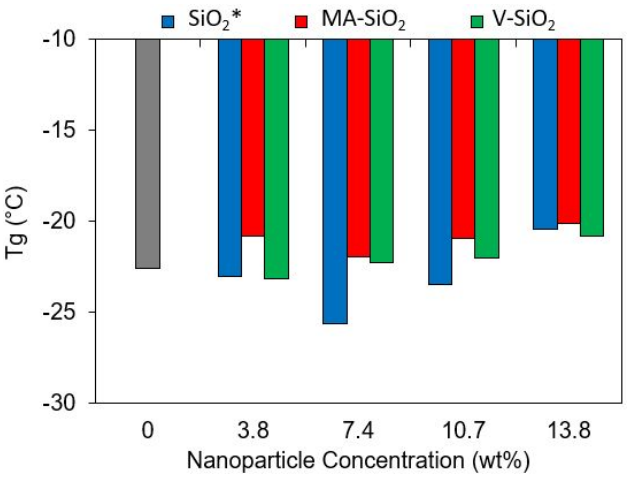

Figure 10. Glass transition temperature measured by DSC at varying nanoparticle weight percentages of SiO_2,[44] MA-SiO_2, and V-SiO_2 nanoparticles.

Further thermomechanical characterization was conducted by measuring storage modulus versus temperature through DMA experiments (**Figure 11**). The DMA curves reveal characteristic thermoset behavior with a glassy plateau at low temperatures, a single step-change in modulus as the temperature passes through the composite T_g, followed by an extended rubbery plateau. The storage modulus in the glassy plateau is on the order of ~1 GPa for all of the samples with no distinct trends for increasing nanoparticle concentration. The rubbery plateau modulus ranges from ~10–40 MPa for all of the samples. Interestingly, the MA-SiO_2 composites displayed a relatively small range of rubbery plateau moduli, while the V-SiO_2 composites showed large variations in rubbery plateau moduli. Both composite series exhibit a decrease in plateau modulus upon the initial addition of nanoparticles, which is attributed to the decrease in gel fraction noted above. For the V-SiO_2 composite series, the initial dip in modulus is more drastic than the MA-SiO_2 series caused by a more substantial decrease in gel fraction for the V-SiO_2 composite. For both sample series, the rubbery plateau modulus increased up to a nanoparticle concentration of 10.7 wt%, but further addition to achieve 13.8 wt% caused a decrease in the rubbery plateau modulus. Next, the storage modulus at 20 °C was extracted and

used to calculate the molecular weight between crosslinks (M_c) using the theory of rubber elasticity.[72–74] As seen in **Table 1**, the sample containing no nanoparticles has a M_c of 96 g/mol, which is less than the molecular weight (575 g/mol) of the pure PEGDA. The shorter M_c is a result of the noncovalent interactions (hydrogen bonding, dipole-dipole bonds, induced dipoles, etc.) that occur in addition to the covalent crosslinking reaction as seen in other studies from Wang et al., Long et al., and Xue et al.[75–77] **Table 1** also reveals that for both MA-SiO_2 and V-SiO_2 nanocomposite series, the M_c gradually decreased with higher loadings of nanoparticles until the weight fraction reaches 10.7 wt%. Thereafter, the molecular weight increases with the addition of 13.8 wt%. The general decrease in M_c is attributed to the covalent bonds formed between the functional end groups on the nanoparticles and the PEGDA monomer. The increase in M_c at 13.8 wt% is predicted to be due to reaching a percolation threshold wherein nanoparticle aggregation begins to occur. Additionally, it was noted that the MA-SiO_2 nanocomposites possess lower M_cs compared to the V-SiO_2 nanocomposites, allowing us to infer that there are more crosslinks in the thermoset creating a tighter network.

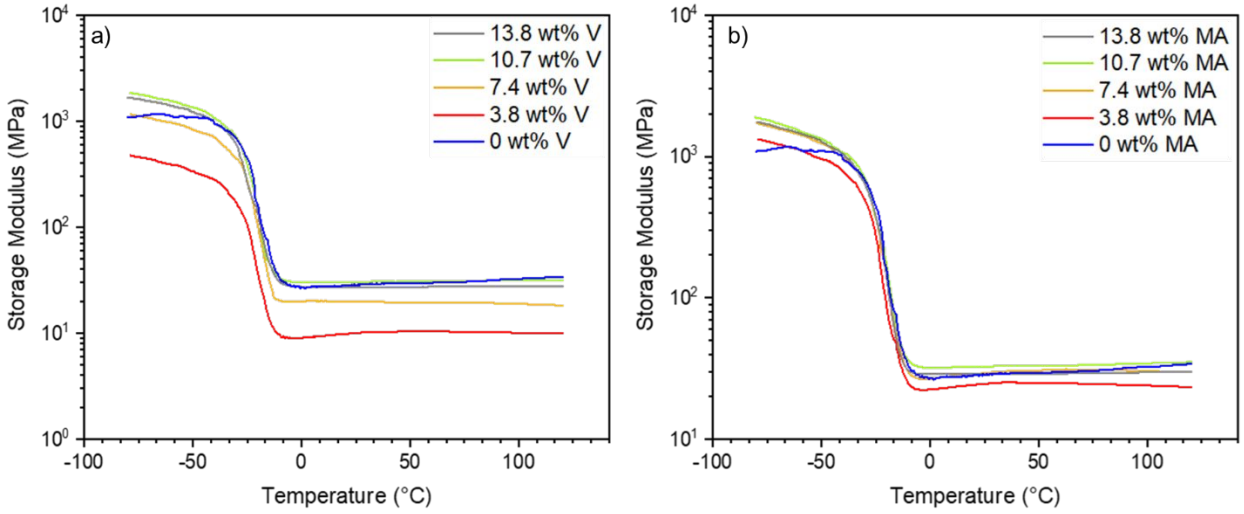

Figure 11. Storage modulus (E') versus temperature measured by DMA at varying nanoparticle weight percentages of a) V-SiO_2 and b) MA-SiO_2.

Table 1. Summary of T_g measured by DSC and DMA, E' at 20 ˚C, and M_c for both MA-SiO_2 and V-SiO_2 loaded composite series.

Functionalized Nanoparticle Concentration (wt%)	MA-SiO_2				V-SiO_2			
	DSC T_g (°C)	DMA T_g (°C)	E' at 20 °C (MPa)	Calculated M_c (g/mol)	DSC T_g (°C)	DMA T_g (°C)	E' at 20 °C (MPa)	Calculated M_c (g/mol)
0	-22.6	-15.5	28.3	96	-22.6	-15.5	28.3	96
3.8	-20.8	-18.9	24.2	113	-23.1	-18.9	9.8	277
7.4	-22.0	-17.4	28.9	94	-22.3	-18.1	19.9	137
10.7	-20.9	-18.1	32.6	84	-22.0	-18.7	30.4	90
13.8	-20.1	-18.5	28.8	95	-20.8	-18.7	27.2	100

The mechanical properties of the nanocomposites were further probed using static strain rate compression tests. From the stress-strain curves, the Young's modulus (**Figure 12a**), the ultimate compressive stress (**Figure 12b**), and the ultimate compressive strain (**Figure 12c**) were determined. The slopes of the stress-strain curves at low values of strain were fit to ascertain the Young's modulus. First, the addition of both V-SiO_2 and MA-SiO_2 nanoparticles dramatically improved the mechanical properties of the composite relative to the unfunctionalized SiO_2. This

further corroborates our prediction that the nanoparticles are chemically reacting with monomers to form crosslinks. Moreover, the Young's modulus of the composite was impacted by the loading of nanoparticles.

For the V-SiO_2 nanoparticles, the Young's modulus exhibits a statistically significant increase with the addition of particles until a concentration of 10.7 wt% is achieved. The data suggests that 10.7 wt% V-SiO_2 is the threshold for the composite in terms of mechanical properties, because >10.7 wt% induces a plateau in the modulus. Similarly, the MA-SiO_2 series displays a statistically significant trend in Young's modulus increase up to a nanoparticle concentration of 10.7 wt%. The MA-SiO_2 nanocomposites reach a threshold of ~325 MPa for the Young's modulus at 10.7 wt%, and then do not change significantly with further addition of particles (13.8 wt%). Without the presence of particle-monomer crosslinks, there is no other explanation for this dramatic increase in Young's modulus and ultimate compressive stress.

A similar trend is seen in the ultimate compressive stress (**Figure 12b**) as the nanocomposites containing V-SiO_2 reach a threshold of ~54 MPa at 10.7 wt%. Once 10.7 wt%, is achieved, the V-SiO_2 nanoparticles no longer elucidate stronger mechanical performance of the composite as there is no statistically significant change in the ultimate compressive stress. For the ultimate compressive stress of MA-SiO_2 nanocomposites, the mechanical strength reaches a maximum at 7.4 wt% with a value of ~74 MPa. With further addition of MA-SiO_2 nanoparticles (>7.4 wt%), the ultimate compressive stress did not incur any significant changes. Having more nanoparticle-monomer crosslinks contributes to a shorter M_c, which causes the stiffness of the composite to increase.[72] Thereby, the MA-SiO_2 nanocomposites reach their ultimate compressive stress threshold at a lower concentration. Wang et al. observed a similar phenomenon in which an increased crosslink density contributed to a higher storage modulus despite a relatively

constant T_g.[72] This also explains why the storage modulus and ultimate compressive stress of the composites containing MA-SiO_2 are generally higher than that of the V-SiO_2.

The ultimate compressive strain at fracture was determined for each composite sample. Upon running statistical analysis for both composite series, it was found that both the MA-SiO_2 and V-SiO_2 containing samples exhibited no significant changes in ultimate compressive stress as a function of nanoparticle concentration. While the trend may not be statistically significant, the V-SiO_2 loaded samples did show a gradual increase in ultimate compressive stress with increasing nanoparticle concentration until the threshold of 7.4 wt% V-SiO_2 nanoparticles was achieved. Thereafter, the ultimate compressive stress decreases with further loadings (>7.4 wt%). These findings are in line with the DMA results that showed no clear trend in the Mc values as a function of nanoparticle loading for either nanoparticle additive.

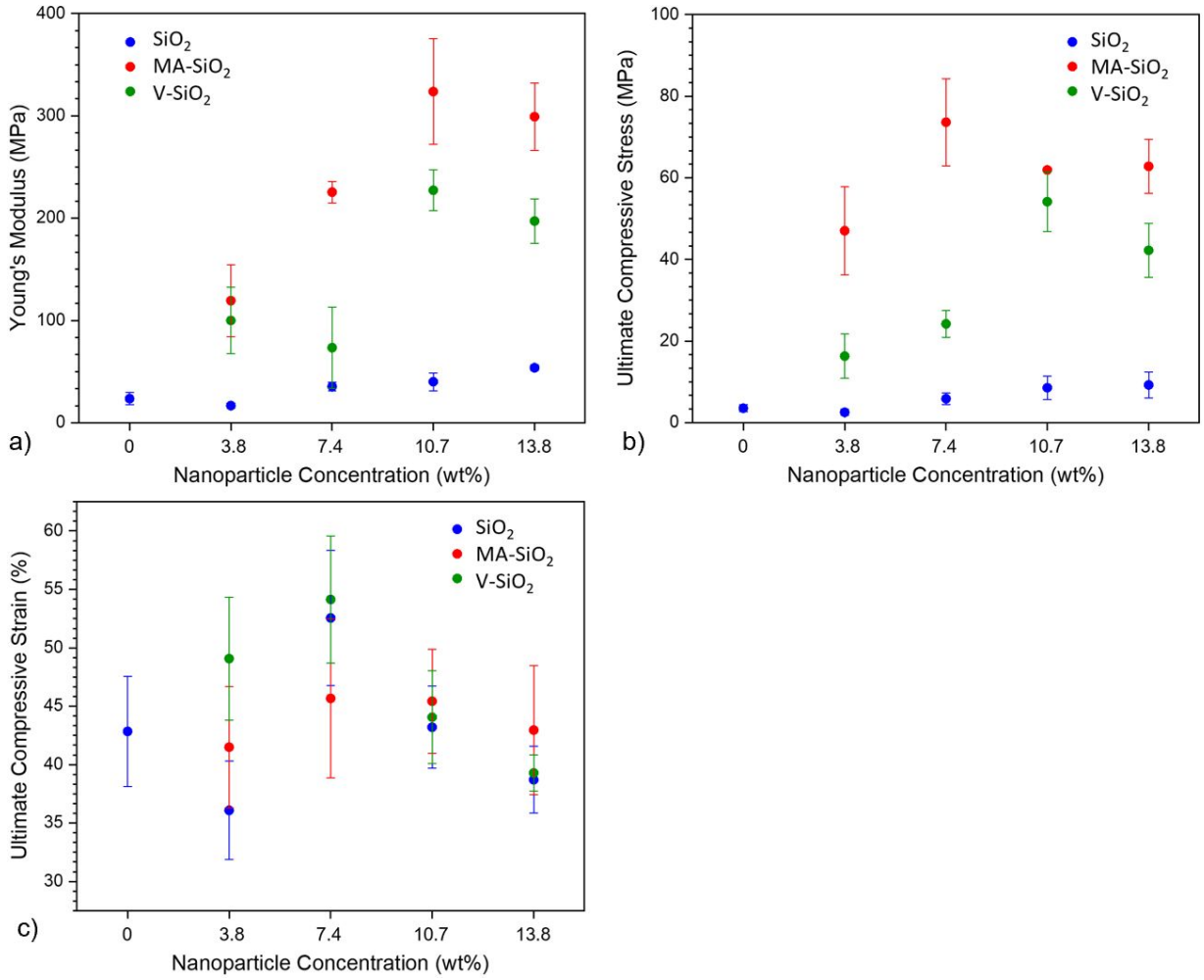

Figure 12. (a) Young's modulus, (b) ultimate compressive stress and (c) ultimate compressive strain, as a function of nanoparticle concentration (wt%) for SiO_2,[44] MA-SiO_2, and V-SiO_2. The data shown are the mean of four independent samples and the error bars represent the standard deviation of the data collected.

Table 2. Summary of Gel Fraction, Water Uptake, Young's Modulus, and Ultimate Compressive Stress and Strain the MA-SiO_2 loaded nanocomposite series. The data shown are the mean of four independent samples and the error bars represent the standard deviation of the data collected.

MA-SiO_2 Nanoparticle (wt%)	Gel Fraction (%)	Water Uptake (%)	Young's Modulus (MPa)	Ultimate Compressive Stress (MPa)	Ultimate Compressive Strain (%)
0	98.0 ± 2.3	36.9 ± 4.7	23.6 ± 5.9	3.5 ± 0.9	42.8 ± 4.7
3.8	97.3 ± 2.2	35.8 ± 2.6	119.3 ± 35.0	47.0 ± 10.8	41.5 ± 5.2
7.4	97.4 ± 1.8	34.1 ± 1.8	225.4 ± 10.4	73.6 ± 10.7	45.7 ± 6.8
10.7	96.4 ± 1.4	33.5 ± 0.8	323.7 ± 51.6	61.9 ± 0.5	45.4 ± 4.5
13.8	98.2 ± 1.0	32.9 ± 3.4	299.2 ± 32.8	62.8 ± 6.6	43.0 ± 5.5

Table 3. Summary of Gel Fraction, Water Uptake, Young's Modulus, and Ultimate Compressive Stress and Strain the V-SiO_2 loaded nanocomposite series. The data shown are the mean of four independent samples and the error bars represent the standard deviation of the data collected.

V-SiO_2 Nanoparticle (wt%)	Gel Fraction (%)	Water Uptake (%)	Young's Modulus (MPa)	Ultimate Compressive Stress (MPa)	Ultimate Compressive Strain (%)
3.8	94.9 ± 1.0	39.0 ± 4.2	112.3 ± 28.6	16.3 ± 5.4	49.1 ± 5.3
7.4	96.5 ± 0.9	40.2 ± 2.9	117.8 ± 12.9	24.2 ± 3.3	54.1 ± 5.5
10.7	99.8 ± 0.5	35.2 ± 6.0	236.5 ± 13.9	54.2 ± 7.3	44.1 ± 4.0
13.8	96.6 ± 2.6	34.8 ± 3.7	185.1 ± 6.5	42.2 ± 6.6	39.3 ± 1.5

Conclusions

PEG nanocomposites containing V-SiO_2 and MA-SiO_2 nanoparticles demonstrate promising characteristics for bioengineering, advanced manufacturing, and multifunctional materials. The introduction of higher concentrations of V-SiO_2 contributed to an increased gel fraction and generally higher Young's modulus and ultimate compressive stress. MA-SiO_2 induced no significant changes in gel fraction with varying particle loading but did cause a general increase in Young's modulus and ultimate compressive stress. While both series caused a dramatic increase in Young's modulus and ultimate compressive stress compared to the unfunctionalized SiO_2, each series reached an ultimate compressive stress threshold at different nanoparticles concentrations. For V-SiO_2, the maximum ultimate compressive stress was observed at 10.7 wt%, while the MA-SiO_2 reached its threshold at a lower concentration of 7.4 wt%. This is predicted to be a result of a shorter molecular weight between crosslinks in composites containing MA-SiO_2, which thereby causes an increase in storage modulus. For both series, the water uptake experiments revealed no statistically significant changes in swelling as function of particle concentration. A similar trend was observed for the T_g of both composite series.

Morphological characterization by SAXS, TEM, and SEM revealed complex behavior dependent both on surface chemistry and on nanoparticle size distribution. When 104 nm diameter SiO_2 nanoparticles were functionalized with the methacrylate ligand, although small aggregates were observed, dispersion was generally good at all loading levels. When nanoparticles having a bimodal size distribution of 93 nm and 12 nm particle diameters were functionalized with a vinyl-based ligand, nanoparticle dispersion in the PEG matrix was generally poor, with large, dense aggregates observed frequently. These results underscore the potential for using similar chemistries on the surface of nanoparticles and in the matrix to improve nanoparticle dispersion in nanocomposites. In summary, nanocomposites containing V-SiO_2 and MA-SiO_2 nanoparticles gives way to an increase in resolution and range of properties that can be selected when creating a tunable and multifunctional material. The results found in this study demonstrate the material's tunability and its applicability to be used in 3D-printed and hierarchical assemblies.

Conflicts of Interest

There are no conflicts of interest to declare.

Acknowledgements

This work was supported through a NASA grant awarded to the Arizona/NASA Space Grant Consortium. This work was funded in part by the following awards: NASA ECF 80NSSC18K1508, ARO W911NF-18-1-0412, NSF CBET 1836719, and NSF DMR 1848454. This research used resources of the Advanced Photon Source, a U.S. Department of Energy (DOE) Office of Science User Facility, operated for the DOE Office of Science by Argonne National Laboratory under Contract No. DE-AC02-06CH11357.

Supporting Information

Additional details on equilibrium times for water uptake, cross-section SEM images, DSC thermograms, tan delta DMA curves, representative stress-strain curves, and AFM images.

References

1. Hamid ZAA, Lim KW. Evaluation of UV-crosslinked poly (ethylene glycol) diacrylate/poly (dimethylsiloxane) dimethacrylate hydrogel: properties for tissue engineering application. *Procedia Chem*. 2016;19:410-418.

2. Kumar SK, Benicewicz BC, Vaia RA, Winey KI. 50th anniversary perspective: are polymer nanocomposites practical for applications? *Macromolecules*. 2017;50(3):714-731.

3. Balazs AC, Emrick T, Russell TP. Nanoparticle Polymer Composites: Where Two Small Worlds Meet. *Science (80-)*. 2006;314(5802):1107-1110. doi:10.1126/science.1130557

4. Osaka I, Abe T, Shimawaki M, Koganezawa T, Takimiya K. Naphthodithiophene-based donor–acceptor polymers: versatile semiconductors for OFETs and OPVs. *ACS Macro Lett*. 2012;1(4):437-440.

5. Crosby AJ, Lee J. Polymer nanocomposites: the “nano” effect on mechanical properties. *Polym Rev*. 2007;47(2):217-229.

6. Ramasubramaniam R, Chen J, Liu H. Homogeneous carbon nanotube/polymer composites for electrical applications. *Appl Phys Lett*. 2003;83(14):2928-2930.

7. Chen H, Ginzburg V V, Yang J, et al. Thermal conductivity of polymer-based composites:

Fundamentals and applications. *Prog Polym Sci*. 2016;59:41-85.

8. Thakur VK, Thakur MK, Raghavan P, Kessler MR. Progress in green polymer composites from lignin for multifunctional applications: a review. *ACS Sustain Chem Eng*. 2014;2(5):1072-1092.

9. Holbery J, Houston D. Natural-fiber-reinforced polymer composites in automotive applications. *Jom*. 2006;58(11):80-86.

10. Astrom BT. *Manufacturing of Polymer Composites*. CRC press; 1997.

11. Englebienne P, Van Hoonacker A. Gold–conductive polymer nanoparticles: A hybrid material with enhanced photonic reactivity to environmental stimuli. *J Colloid Interface Sci*. 2005;292(2):445-454. doi:http://dx.doi.org/10.1016/j.jcis.2005.06.001

12. Oh Y, Chun K-Y, Lee E, Kim Y-J, Baik S. Functionalized nano-silver particles assembled on one-dimensional nanotube scaffolds for ultra-highly conductive silver/polymer composites. *J Mater Chem*. 2010;20(18):3579-3582. doi:10.1039/C0JM00086H

13. Turhan Y, Dogan M, Alkan M. Poly (vinyl chloride)/kaolinite nanocomposites: characterization and thermal and optical properties. *Ind Eng Chem Res*. 2010;49(4):1503-1513.

14. Huang X-J, Zeng X-F, Wang J-X, Chen J-F. Transparent dispersions of monodispersed ZnO nanoparticles with ultrahigh content and stability for polymer nanocomposite film with excellent optical properties. *Ind Eng Chem Res*. 2018;57(12):4253-4260.

15. Das TK, Prusty S. Graphene-based polymer composites and their applications. *Polym Plast Technol Eng*. 2013;52(4):319-331.

16. Linares A, Canalda JC, Cagiao ME, et al. Broad-band electrical conductivity of high density polyethylene nanocomposites with carbon nanoadditives: multiwall carbon nanotubes and carbon nanofibers. *Macromolecules*. 2008;41(19):7090-7097.

17. Katoueizadeh E, Zebarjad SM, Janghorban K. Synthesis and enhanced visible-light activity of N-doped TiO2 nano-additives applied over cotton textiles. *J Mater Res Technol*. 2018;7(3):204-211.

18. Kumar SK, Krishnamoorti R. Nanocomposites: structure, phase behavior, and properties. *Annu Rev Chem Biomol Eng*. 2010;1:37-58.

19. Oberdisse J. Aggregation of colloidal nanoparticles in polymer matrices. *Soft Matter*. 2006;2(1):29-36.

20. Billiet L, Fournier D, Du Prez F. Step-growth polymerization and 'click'chemistry: The oldest polymers rejuvenated. *Polymer (Guildf)*. 2009;50(16):3877-3886.

21. Yilmaz G, Yagci Y. Light-induced step-growth polymerization. *Prog Polym Sci*. 2020;100:101178.

22. Stille JK. Step-growth polymerization. 1981.

23. Vilela C, Sousa AF, Fonseca AC, et al. The quest for sustainable polyesters–insights into the future. *Polym Chem*. 2014;5(9):3119-3141.

24. Soudagar MEM, Nik-Ghazali N-N, Kalam MA, Badruddin IA, Banapurmath NR, Akram N. The effect of nano-additives in diesel-biodiesel fuel blends: A comprehensive review on stability, engine performance and emission characteristics. *Energy Convers Manag*. 2018;178:146-177.

25. Hossain N, Mahlia TMI, Saidur R. Latest development in microalgae-biofuel production with nano-additives. *Biotechnol Biofuels*. 2019;12(1):1-16.

26. Hata E, Mitsube K, Momose K, Tomita Y. Holographic nanoparticle-polymer composites based on step-growth thiol-ene photopolymerization. *Opt Mater Express*. 2011;1(2):207-222.

27. Matyjaszewski K, Davis TP. *Handbook of Radical Polymerization*. John Wiley & Sons; 2003.

28. Hawker CJ. Molecular weight control by a" living" free-radical polymerization process. *J Am Chem Soc*. 1994;116(24):11185-11186.

29. Song SW, Jeong Y, Kwon S. Photocurable polymer nanocomposites for magnetic, optical, and biological applications. *IEEE J Sel Top Quantum Electron*. 2014;21(4):324-335.

30. Moriche R, Artigas J, Reigosa L, Sánchez M, Prolongo SG, Ureña A. Modifications induced in photocuring of Bis-GMA/TEGDMA by the addition of graphene nanoplatelets for 3D printable electrically conductive nanocomposites. *Compos Sci Technol*. 2019;184:107876.

31. Martin-Gallego M, Hernández M, Lorenzo V, Verdejo R, Lopez-Manchado MA, Sangermano M. Cationic photocured epoxy nanocomposites filled with different carbon fillers. *Polymer (Guildf)*. 2012;53(9):1831-1838.

32. Dizon JRC, Chen Q, Valino AD, Advincula RC. Thermo-mechanical and swelling properties of three-dimensional-printed poly (ethylene glycol) diacrylate/silica nanocomposites. *MRS Commun*. 2019;9(1):209-217.

33. Mohamadpour S, Pourabbas B, Fabbri P. Anti-scratch and adhesion properties of photo-curable polymer/clay nanocomposite coatings based on methacrylate monomers. *Sci Iran*. 2011;18(3):765-771.

34. Lakes R. Materials with structural hierarchy. *Nature*. 1993;361(6412):511-515.

35. Chia HN, Wu BM. Recent advances in 3D printing of biomaterials. *J Biol Eng*. 2015;9(1):1-14.

36. Ligon-Auer SC, Schwentenwein M, Gorsche C, Stampfl J, Liska R. Toughening of photo-curable polymer networks: a review. *Polym Chem*. 2016;7(2):257-286.

37. Pavlinec J, Moszner N. Photocured polymer networks based on multifunctional β-ketoesters and acrylates. *J Appl Polym Sci*. 1997;65(1):165-178.

38. Sadej M, Gojzewski H, Andrzejewska E. Photocurable polymethacrylate-silica nanocomposites: correlation between dispersion stability, curing kinetics, morphology and properties. *J Polym Res*. 2016;23(6):1-11.

39. Soloukhin VA, Posthumus W, Brokken-Zijp JCM, Loos J, de With G. Mechanical properties of silica–(meth) acrylate hybrid coatings on polycarbonate substrate. *Polymer (Guildf)*. 2002;43(23):6169-6181.

40. Potapov V V, Shitikov ES, Trutnev NS, Gorbach VA, Portnyagin NN. Influence of silica nanoparticles on the strength characteristics of cement samples. *Glas Phys Chem*. 2011;37(1):98-105.

41. Grigoriadou I, Nianias N, Hoppe A, et al. Evaluation of silica-nanotubes and strontium hydroxyapatite nanorods as appropriate nanoadditives for poly (butylene succinate)

biodegradable polyester for biomedical applications. *Compos Part B Eng*. 2014;60:49-59.

42. Miyata T, Nagao T, Watanabe D, et al. Nanoscale Stress Distribution in Silica-Nanoparticle-Filled Rubber as Observed by Transmission Electron Microscopy: Implications for Tire Application. *ACS Appl Nano Mater*. 2021.

43. Liu Y-L, Hsu C-Y, Wei W-L, Jeng R-J. Preparation and thermal properties of epoxy-silica nanocomposites from nanoscale colloidal silica. *Polymer (Guildf)*. 2003;44(18):5159-5167.

44. Hocken A, Yang Y, Beyer FL, et al. Photocurable poly (ethylene glycol) diacrylate resins with variable silica nanoparticle loading. *Ind Eng Chem Res*. 2019.

45. Kumar P, Sandeep KP, Alavi S, Truong VD. A review of experimental and modeling techniques to determine properties of biopolymer-based nanocomposites. *J Food Sci*. 2011;76(1):E2-E14.

46. Jancar J, Douglas JF, Starr FW, et al. Current issues in research on structure–property relationships in polymer nanocomposites. *Polymer (Guildf)*. 2010;51(15):3321-3343.

47. Schneider G, Decher G. Functional core/shell nanoparticles via layer-by-layer assembly. Investigation of the experimental parameters for controlling particle aggregation and for enhancing dispersion stability. *Langmuir*. 2008;24(5):1778-1789.

48. Rossi F, Ferrari R, Castiglione F, Mele A, Perale G, Moscatelli D. Polymer hydrogel functionalized with biodegradable nanoparticles as composite system for controlled drug delivery. *Nanotechnology*. 2014;26(1):15602.

49. Jia X, Li Y, Cheng Q, Zhang S, Zhang B. Preparation and properties of poly (vinyl

alcohol)/silica nanocomposites derived from copolymerization of vinyl silica nanoparticles and vinyl acetate. *Eur Polym J*. 2007;43(4):1123-1131.

50. Akbari A, Yegani R, Pourabbas B. Synthesis of high dispersible hydrophilic poly (ethylene glycol)/vinyl silane grafted silica nanoparticles to fabricate protein repellent polyethylene nanocomposite. *Eur Polym J*. 2016;81:86-97.

51. Shin Y, Lee D, Lee K, Ahn KH, Kim B. Surface properties of silica nanoparticles modified with polymers for polymer nanocomposite applications. *J Ind Eng Chem*. 2008;14(4):515-519. doi:https://doi.org/10.1016/j.jiec.2008.02.002

52. Matias T, Varino C, de Sousa HC, et al. Novel flexible, hybrid aerogels with vinyl-and methyltrimethoxysilane in the underlying silica structure. *J Mater Sci*. 2016;51(14):6781-6792.

53. Zou H, Wu S, Shen J. Polymer/silica nanocomposites: preparation, characterization, properties, and applications. *Chem Rev*. 2008;108(9):3893-3957.

54. Wang Q, Hou R, Cheng Y, Fu J. Super-tough double-network hydrogels reinforced by covalently compositing with silica-nanoparticles. *Soft Matter*. 2012;8(22):6048-6056.

55. Bauer F, Sauerland V, Gläsel H-J, et al. Preparation of Scratch and Abrasion Resistant Polymeric Nanocomposites by Monomer Grafting onto Nanoparticles, 3. Effect of Filler Particles and Grafting Agents. *Macromol Mater Eng*. 2002;287(8):546-552. doi:https://doi.org/10.1002/1439-2054(20020801)287:8<546::AID-MAME546>3.0.CO;2-W

56. Ribeiro T, Baleizão C, Farinha JPS. Functional films from silica/polymer nanoparticles.

Materials (Basel). 2014;7(5):3881-3900.

57. Ilavsky J, Zhang F, Andrews RN, et al. Development of combined microstructure and structure characterization facility for in situ and operando studies at the Advanced Photon Source. *J Appl Crystallogr*. 2018;51(3):867-882.

58. Ilavsky J. Nika: software for two-dimensional data reduction. *J Appl Crystallogr*. 2012;45(2):324-328.

59. Ilavsky J, Jemian PR. Irena: tool suite for modeling and analysis of small-angle scattering. *J Appl Crystallogr*. 2009;42(2):347-353.

60. Kline SR. Reduction and analysis of SANS and USANS data using IGOR Pro. *J Appl Crystallogr*. 2006;39(6):895-900.

61. Liu J, Rad IY, Sun F, Stansbury JW. Photo-reactive nanogels as a means to tune properties during polymer network formation. *Polym Chem*. 2014;5(1):227-233.

62. Fairbanks BD, Scott TF, Kloxin CJ, Anseth KS, Bowman CN. Thiol− yne photopolymerizations: Novel mechanism, kinetics, and step-growth formation of highly cross-linked networks. *Macromolecules*. 2009;42(1):211-217.

63. Roe R-J. *Methods of X-Ray and Neutron Scattering in Polymer Science*. Oxford University Press on Demand; 2000.

64. Schaefer DW, Rieker T, Agamalian M, et al. Multilevel structure of reinforcing silica and carbon. *J Appl Crystallogr*. 2000;33(3):587-591.

65. Glatter O, Kratky O. *Small Angle X-Ray Scattering*. New York: Academic Press; 1982.

66. Fagherazzi G. Small angle X-ray scattering edited by O. Glatter and O. Kratky. *Acta Crystallogr Sect A Found Crystallogr*. 1983;39(3):500.

67. Kane MC, Londono JD, Beyer FL, Brennan AB. Characterization of the hierarchical structures of a dry nanopowder in a polymer matrix by X-ray scattering techniques. *J Appl Crystallogr*. 2009;42(5):925-931.

68. Li T, Senesi AJ, Lee B. Small angle X-ray scattering for nanoparticle research. *Chem Rev*. 2016;116(18):11128-11180.

69. Schaefer DW, Justice RS. How nano are nanocomposites? *Macromolecules*. 2007;40(24):8501-8517.

70. Seelenmeyer S, Deike I, Rosenfeldt S, et al. Small-angle x-ray and neutron scattering studies of the volume phase transition in thermosensitive core–shell colloids. *J Chem Phys*. 2001;114(23):10471-10478.

71. Percus JK, Yevick GJ. Analysis of classical statistical mechanics by means of collective coordinates. *Phys Rev*. 1958;110(1):1.

72. Wang M, Dheressa E, Brown Kristen A, Green Matthew D. Effect of Crosslinker Length and Architecture on the Thermomechanical Properties of CNT-Loaded Elastomeric Polymer Matrix Composites. *Macromol Rapid Commun*. 2018;0(0):1800091. doi:10.1002/marc.201800091

73. Skourlis TP, McCullough RL. An experimental investigation of the effect of prepolymer molecular weight and stoichiometry on thermal and tensile properties of epoxy resins. *J Appl Polym Sci*. 1996;62(3):481-490.

74. Gluck-Hirsch JB, Kokini JL. Determination of the molecular weight between crosslinks of waxy maize starches using the theory of rubber elasticity. *J Rheol (N Y N Y)*. 1997;41(1):129-140.

75. Wang W, Zhang Y, Liu W. Bioinspired fabrication of high strength hydrogels from non-covalent interactions. *Prog Polym Sci*. 2017;71:1-25.

76. Long TR, Elder RM, Bain ED, et al. Influence of molecular weight between crosslinks on the mechanical properties of polymers formed via ring-opening metathesis. *Soft Matter*. 2018;14(17):3344-3360.

77. Xue K, Liow SS, Karim AA, Li Z, Loh XJ. A recent perspective on noncovalently formed polymeric hydrogels. *Chem Rec*. 2018;18(10):1517-1529.